Overcoming Efficiency Limits of Carbon Nanotube –Laminated Metal-free Perovskite Solar Cells

Jin-Wook Lee[‡1], Il Jeon[‡2], Haosheng Lin[2], Seungjoo Seo[2], Tae-Hee Han[1], Anton Anisimov[3], Esko I. Kauppinen[4], Yutaka Matsuo[2], Shigeo Maruyama*[2,5], Yang Yang*[1]*

[1]Department of Materials Science and Engineering and California Nano Systems Institute, University of California, Los Angeles, CA 90095, United States

[2]Department of Mechanical Engineering, School of Engineering, The University of Tokyo, Tokyo 113-8656, Japan

[3]Canatu, Ltd., Konalankuja 5, FI-00390 Helsinki, Finland

[4]Department of Applied Physics, Aalto University School of Science, FI-00076 Aalto, Finland

[5]Energy Nano Engineering Laboratory, National Institute of Advanced Industrial Science and Technology (AIST), Ibaraki 305-8564, Japan

[‡]These authors contributed equally to this work.

*Corresponding author

Y. M. E-mail: matsuo@photon.t.u-tokyo.ac.jp

S. M. E-mail: maruyama@photon.t.u-tokyo.ac.jp

Y. Y. E-mail: yangy@ucla.edu; TEL: +1-310-825-4052

KEYWORDS : perovskite, solar cell, carbon nanotube, doping, stability

ABSTRACT

Single-walled carbon nanotubes (CNTs) has been considered as a promising material for a top electrode of perovskite solar cells owing to its hydrophobic nature, earth-abundance, and mechanical robustness. However, its poor conductivity, a shallow work function, and non-reflective nature have limited further enhancement in power conversion efficiency (PCE) of top CNT electrode-based perovskite solar cells. Here, we introduced a simple, quick, and scalable method to address these issues by utilizing an ex-situ vapor-assisted doping method. Trifluoromethanesulfonic acid (TFMS) vapor doping of the free-standing CNT sheet enabled tuning of conductivity and work function of the CNT electrode without damaging underneath layers. The sheet resistance of the CNT sheet was decreased by 21.3% with an increase in work function from 4.75 eV to 4.96 eV upon doping of TFMS. In addition, recently developed 2D perovskite-protected Cs-containing formamidium lead iodide ($FACsPbI_3$) technology was employed to maximize the absorption. Because of the lowered resistance, better energy alignment, and improved absorption, the CNT electrode-based PSCs produced a PCE of 17.6% with a J_{SC} of 24.21 mA cm^{-2}, V_{OC} of 1.005 V, and FF of 0.72. The obtained PCE is the record-high efficiency among the reported CNT top electrode-based PSCs. Furthermore, the resulting TFMS-doped CNT-PSCs demonstrated higher thermal and operational stability than bare CNT and metal electrode-based devices.

TABLE OF CONTENT

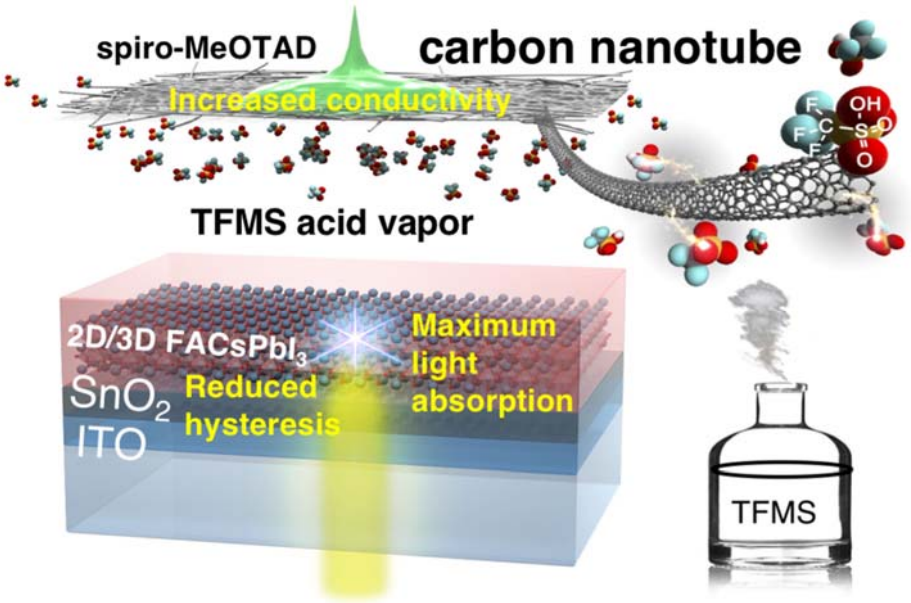

INTRODUCTION

Perovskite solar cells (PSCs), reported by Miyasaka and colleagues for the first time in 2009,[1-2] have progressed remarkably through a heated power conversion efficiency (PCE) race.[3-4] With a surge of research efforts, the certified PCE of the lab scale PSCs increased from 14.1% to 22.7% for last 5 years, which is on par with silicon and CIGS solar cells.[5] Now the research efforts are being focused on enhancing the durability of the devices and reducing the production cost.

PSCs are usually fabricated on transparent conducting oxide (TCO) glass substrates where the perovskite layer is sandwiched between additional selective charge transporting layers. Typically, a metal electrode is thermally evaporated on top to serve as a counter electrode. These top metal electrodes, however, are known to substantially increase the process and material cost as expensive gold or silver layers are deposited under high vacuum.[6-7] Furthermore, the metal electrodes are found to be not robust enough to render long-term stability of the PSCs as the metal ions migrate into the bulk of the device under an operational condition to react with the active materials, thus degrading the device.[8-9]

As an alternative to the metal electrodes, researchers have incorporated single-walled carbon nanotubes (CNTs) into the PSC system. The CNT is a favorable electrode material, owing to its hydrophobic nature, earth-abundance, and mechanical robustness. The application of CNT realizes CNT-based PSCs with good stability and versatility.[10-13] Among the reported CNT-used PSCs devices, aerosol-synthesized CNT top electrode (or back electrode)[14-15] replacing metals in PSCs has shown the most promising potential.[16-17] The application of CNT as the top electrode substantially enhances the stability of PSCs by removing the ion migration,[18] and drastically reduces the fabrication cost as it can be easily deposited onto devices by a simple mechanical transfer.[19] Despite such advantages, there are three factors limiting the PCE of the CNT top

electrode-based PSCs that need to be addressed: 1) the work function of the CNT does not align with the perovskite, leading to loss in voltage potential 2) CNT top electrode is less conductive than the metal counterparts, limiting the fill factor (FF) of the devices 3) the CNT back electrode is not reflective that the devices cannot maximize the light harvesting short-circuit current.

In this work, we addressed those three issues by engineering CNT electrode and photo-active layer. We tuned the work function of CNT electrodes and increased their conductivity by using a vapor-assisted doping of trifluoromethanesulfonic acid (TFMS). Furthermore, by incorporation of low bandgap 2D perovskite-protected Cs-containing formamidium lead iodide (2D/3D $FACsPbI_3$),[ref of UCLA submitted paper] we enabled the harvesting of long-wavelength light, enhancing the photocurrent of the devices. By combining those technologies all into one device system, CNT electrode-based PSCs produced a PCE of 17.6% with a J_{SC} of 24.21 mA cm^{-2}, V_{OC} of 1.005 V, and FF of 0.72. The obtained PCE is the highest among the values reported from CNT top electrode-based PSCs. Moreover, the resulting CNT-PSCs exhibited higher high-temperature operational stability than those of the devices based on metal electrodes as well as conventional CNT electrodes.

RESULTS AND DISCUSSION

Doping carbon top electrode in solar cells is an extremely challenging task and there has been only one report to the best our knowledge.[20] This is because acid solution used for doping damages the layers underneath. In this work, we achieved a successful doping of CNT top electrode without damaging the device. We achieved this by using vapor doping of highly effective and durable TFMS.[21] The TFMS chemical *p*-dopant is known to dope carbon electrodes more effectively with a much longer durability than conventional HNO_3.[20] By simply placing a sheet of CNT film on

TFMS vapor for several tens of seconds, we can achieve the doping (**Figure 1a**). The degree of doping can be controlled by the exposure time of the CNT sheet to TFMS vapor (the doping time was varied from 10 to 50 s). After cutting the CNT film into a designated pattern, we laminated TFMS-doped CNT film onto the 2D/3D $FACsPbI_3$ perovskite film. It is worth noting that too much force during the lamination step caused cracks to appear in the perovskite film from which an electrical short circuit occurs (**Figure S1**). Such phenomenon was not observed with methylammonium lead iodide ($MAPbI_3$) and unique to 2D/3D $FACsPbI_3$. After the transfer, we peeled off the nitrocellulose film, and applied spiro-MeOTAD solution to improve the contact between the CNTs and the perovskite and to enhance the charge selectivity of the CNTs.

The four-probe measurement was used to measure the sheet resistance of the CNT films upon TFMS vapor doping. According to **Figure 1b**, the bare CNT film has a sheet resistance of approximately 153.9 Ω sq^{-1}. We can observe that the sheet resistance decreases with an increase in the TFMS vapor doping time. There is a particularly sharp decrease in the sheet resistance from 30 s to 40 s of the doping time, followed by almost saturation of the sheet resistance with the doping time longer than 40 s. The sheet resistance decreased from 153.9 to 150.5 (2.2% decrease), 147.9 (2.7% decrease), 139.1 (9.6% decrease), 121.1 (21.3%) and 120.5 Ω sq^{-1} (21.7%) for 10, 20, 30, 40 and 50 s of doping time, respectively. Although the decrease in the sheet resistance is not as great as the reported drop-cast doping method,[20] this ex-situ vapor-assisted doping method successfully induces doping of the top-laminated CNT films without damaging the layers underneath. Vis–NIR optical absorbance spectroscopy can also show the *p*-type doping effect of CNTs.[22-23] **Figure 1c** reveals that the optical transitions of the van Hove singularities (E^{M}_{11}, E^{S}_{22}, E^{S}_{11}) were slightly quenched after TFMS vapor doping. This indicates that the inter-band optical absorptions were suppressed due to the shift of the Fermi level by the TFMS molecules. The

uniformity of the doping was investigated by elemental distribution analysis in **Figure S2**. The uniform distribution of oxygen and sulfur originating from the TEMS confirms that the doping is microscopically uniform. Raman spectroscopy can also tell us the degree of doping effect. In our case, however, there was no apparent blue shift of the G nor G′ bands of the vapor-doped CNT films (**Figure S3**). This is ascribed to the mild effect of the vapor doping and there have been many cases in which the doping effect was not visible by Raman spectroscopy. [10.1021/jacs.5b03739]

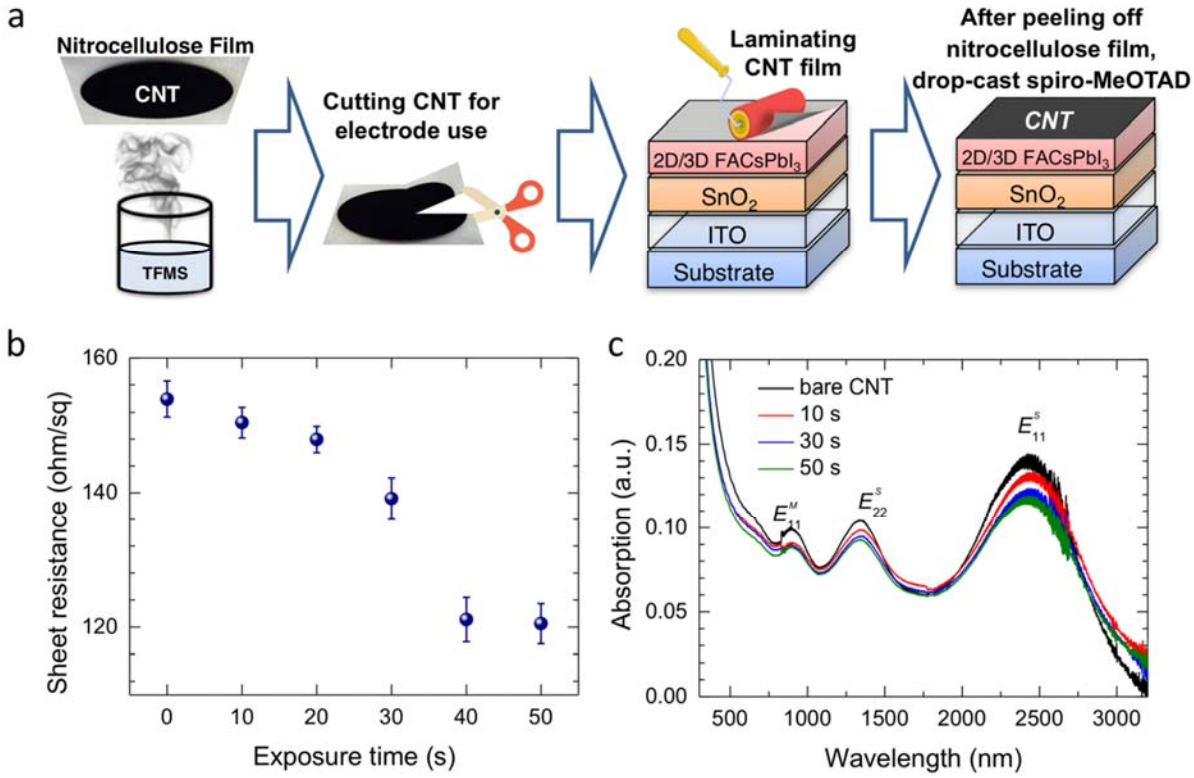

Figure 1. (a) Schematic illustration showing doping and device fabrication processes of carbon nanotube (CNT) doped by using vaporized trifluoromethyl sulfonamide (TFMS) (b) Measured sheet resistance with different exposure time to TFMS vapor. (c) Vis-NIR spectra of bare CNT (black), 10 s vapor-doped CNT (red), 30 s vapor-doped CNT (blue), and 50 s vapor-doped CNT (green).

After investigating the vapor doping effect on CNT, we fabricated CNT-PSCs in a structural configuration of glass/indium tin oxide (ITO)/SnO_2/$FACsPbI_3$/TFMS-doped CNT/spiro-

MeOTAD (**Figure 2a**). $FAPbI_3$ (2D/3D $FACsPbI_3$) has a bandgap of 1.4 eV which theoretically results in the maximum PCE of the Shockley-Queisser limit and higher absorption than conventional $MAPbI_3$ which is critical to CNT top electrode-based PSCs (**Figure S4**). Indeed, 2D/3D $FACsPbI_3$–based CNT PSCs showed a high short-circuit current density (J_{SC}) despite low open circuit voltage (V_{OC}), which may be attributed to unfavorable energy alignment between and 2D/3D $FACsPbI_3$ the CNT electrode (**Table S1**). Upon doping of the CNT with TFMS, all the photovoltaic parameters improved; the J_{SC} increased from 22.73±0.71 to 23.52±0.39 mA/cm^2 (**Figure 2c**, 3.4% increase), the V_{OC} increased from 0.991±0.014 to 1.010±0.014 V (**Figure 2d**, 1.9% increase), and the FF increased from 0.679±0.019 to 0.706±0.016 (**Figure 2e**, 4.0% increase). As a result, the average PCE increased by 9.7% from 15.29±0.46 to 16.77±0.46% (**Figure 2f**). The highest PCE of the device with TFMS-doped CNT reached 17.56% (J_{SC}: 24.21 mA/cm^2, V_{OC}: 1.005V and FF: 0.722), whereas that of the device based on bare CNT showed 15.83% (J_{SC}: 23.35 mA/cm^2, V_{OC}: 0.985V and FF: 0.688). The obtained PCE with 30 s of TFMS doping is the highest among the reported PCEs from CNT top electrode-based PSCs (**Figure S5**). However, the doping time longer than 30 s decreased the device performance to 15.83% (J_{SC}: 22.67 mA/cm^2, V_{OC}: 0.978V and FF: 0.716) (**Table 1**).

Table 1. Photovoltaic performance of metal-free CNT top electrode-based 2D/3D $FACsPbI_3$ PSCs with different TFMS vapor doping time under 1 sun (AM 1.5 G, 100 mW cm^{-2}). The photovoltaic parameters are the best values with averages and error ranges in parentheses.

Device ID	J_{SC} (mA/cm^2) [average]	V_{OC} (V) [average]	FF [average]	PCE (%) [average]
Bare CNT	23.35 [22.73±0.71]	0.985 [0.991±0.014]	0.688 [0.679±0.019]	15.83 [15.29±0.46]
TFMS 30 s	24.21 [23.52±0.39]	1.005 [1.010±0.014]	0.722 [0.706±0.016]	17.56 [16.77±0.46]
TFMS 50 s	22.67	0.978	0.716	15.87

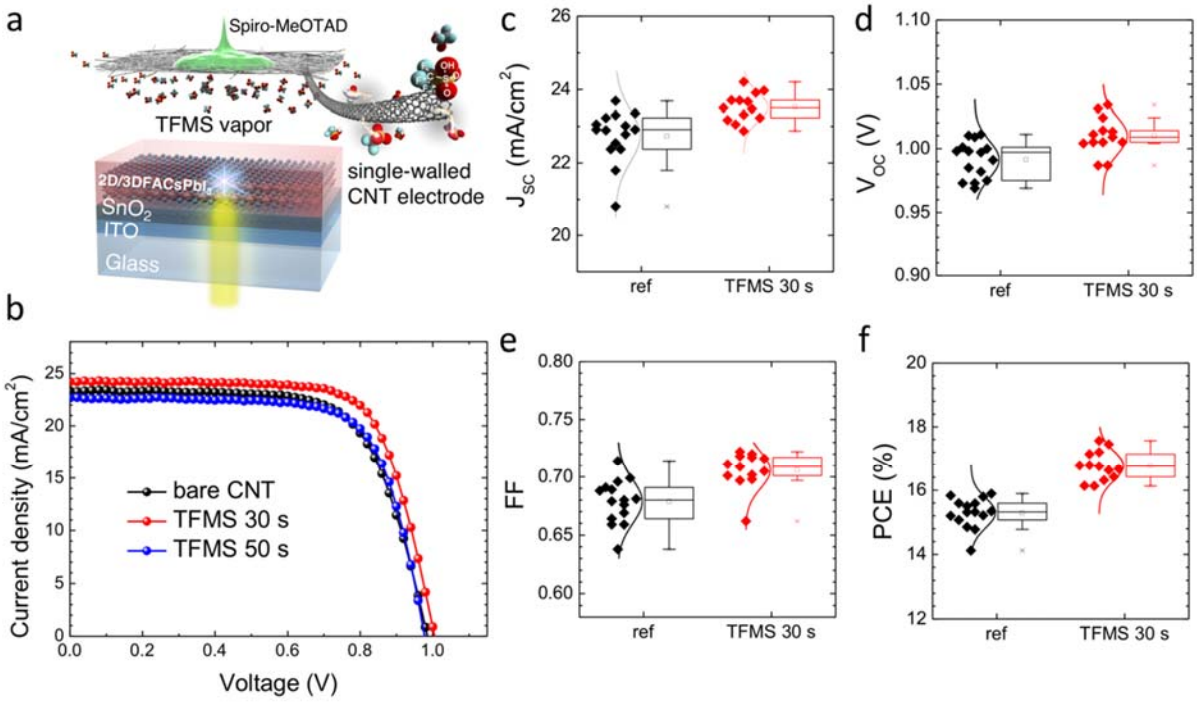

Figure 2. (a) Schematic illustration showing the structure of planar heterojunction perovskite solar cells based on TFMS doped CNT (b) Current density-voltage (*J–V*) curves of the highest efficiency perovskite solar cells incorporating bare CNT and CNT doped by TFMS (30 s and 50 s of doping time). (c) Short-circuit current density (J_{SC}), (d) open circuit voltage (V_{OC}), (e) fill factor (FF) and (f) power conversion efficiency (PCE) of the perovskite solar cells incorporating bare CNT and CNT doped by TFMS.

To elucidate the reasons behind the improved photovoltaic parameters, we investigated the work functions of CNTs and resulting charge extraction properties in a combination of photoelectron yield spectroscopy (PYS) and photoluminescence (PL) analyses. PYS data of the TFMS-doped CNT films show that the Fermi level of CNT decreases with the increase in the TFMS vapor doping time (**Figure 3a**). As the doping time increased, the Fermi level of the CNT shifted from -4.75 eV (bare CNT) to -4.87 eV, -4.96 eV and -5.02 eV for 10 s, 30 s and 50 s doping time, respectively. The higher work functions with the increased doping time can be attributed to the increase in hole concentration, owing to the larger amount of the TFMS adsorption, which is in agreement with the sheet resistance and Vis-NIR measurement in Figure 1. According to the

energy diagram in **Figure 3b**, the higher work function caused by stronger TFMS doping is energetically favorable in reducing the potential loss in terms of hole extraction, which is probably the origin of the enhanced V_{OC}. The charge extraction dynamic was investigated by steady-state and time-resolved PL measurement in **Figure 3c** and **d**, respectively. The bare perovskite film in contact with a glass substrate showed the peak PL intensity of 4.58×10^6, which was significantly quenched to 1.07×10^6 when in contact with bare CNT. With 30 s TFMS doping, the PL quenching became more pronounced where the peak PL intensity was 1.40×10^6, implying better hole extraction capability of the CNT with TFMS doping. The better hole extraction ability after TFMS doping was further confirmed by time-resolved PL decay profiles (**Figure 3d**). The perovskite films in contact with CNT sheets showed the ultrafast decay followed by a slower decay in PL intensity. The ultrafast decay (τ_{HTM}) can be attributed to the PL decay as a result of hole extraction by CNT, whereas the slower decay can be ascribed to the radiative recombination of remaining charges in bulk perovskite. The TFMS doped CNT showed the faster decay of the PL intensity (τ_{HTM}=1.0 ns) with less proportion of remaining tail than that of the perovskite film with bare CNT (τ_{HTM}=1.6 ns), indicating enhanced charge extraction ability with TFMS doping.

Despite the increase in the conductivity of CNT and energetically more favour outcome upon TFMS doping, the device performance decreased when the vapor doping time was longer than 30 s. We hypothesize that this is because of surplus TFMS molecules reacting with the spiro-MeOTAD solution. The spiro-MeOTAD solution contains a small amount of *t*-BP which is a Lewis base with a nitrogen atom. TFMS can undergo an acid-base reaction with *t*-BP (1).[24] This was evidenced by the downshifts of H_a (δ = 8.87 ppm) and H_b (δ = 8.16 ppm) in *t*-BP to H_a (δ = 8.49 ppm) and H_b (δ = 7.39ppm) upon addition of 10 wt% TFMS, according to the ^{1}H NMR data in **Figure 3e**. The change in the coupling constant indicates the change in chemical environment

by the protonation (**Figure S6**). The protonated *t*-BP product precipitated in chlorobenzene as salts do not dissolve in non-polar solvents. The loss of *t*-BP from the spiro-MeOTAD solution leads to the decrease in all photovoltaic parameters for *t*-BP is absolutely necessary to inhibit the complexation and enhance the solubility of spiro-MeOTAD.[25] This explains the decreases in J_{SC}, V_{OC}, and FF of the devices when longer than 30 s of TFMS doping was applied. However, the decreases in V_{OC} and FF were not as big as the J_{SC} drop. This is because while the loss of *t*-BP decreased all photovoltaic parameters, the decrease in the Fermi level and the increased conductivity of CNT countered the drops in V_{OC} and FF. It should be mentioned that both spiro-MeOTAD and LiTFSI also contain nitrogen atoms, which may undergo protonation by TFMS as well.

$$4\text{-}C(CH_3)_3C_5H_4N + CF_3SO_3H \rightleftharpoons [4\text{-}C(CH_3)_3C_5H_4NH]^+[CF_3SO_3]^{-OF} \quad (1)$$

This agrees with the Nyquist plot of 50 s TFMS-treated CNT showing higher counter electrode resistance (R_{CT}, first semi-circle) despite lower series resistance (R_S, starting point of the semi-circle) than either 30 s TFMS-treated CNT and bare CNT on a perovskite film (**Figure S7**).

Therefore, it is of importance to control the amount of TFMS dopants. The optimal amount should be large enough to enhance the conductivity and to lower the Fermi level of the CNT, but small enough to avoid reaction with *t*-BP in the spiro-MeOTAD solution.

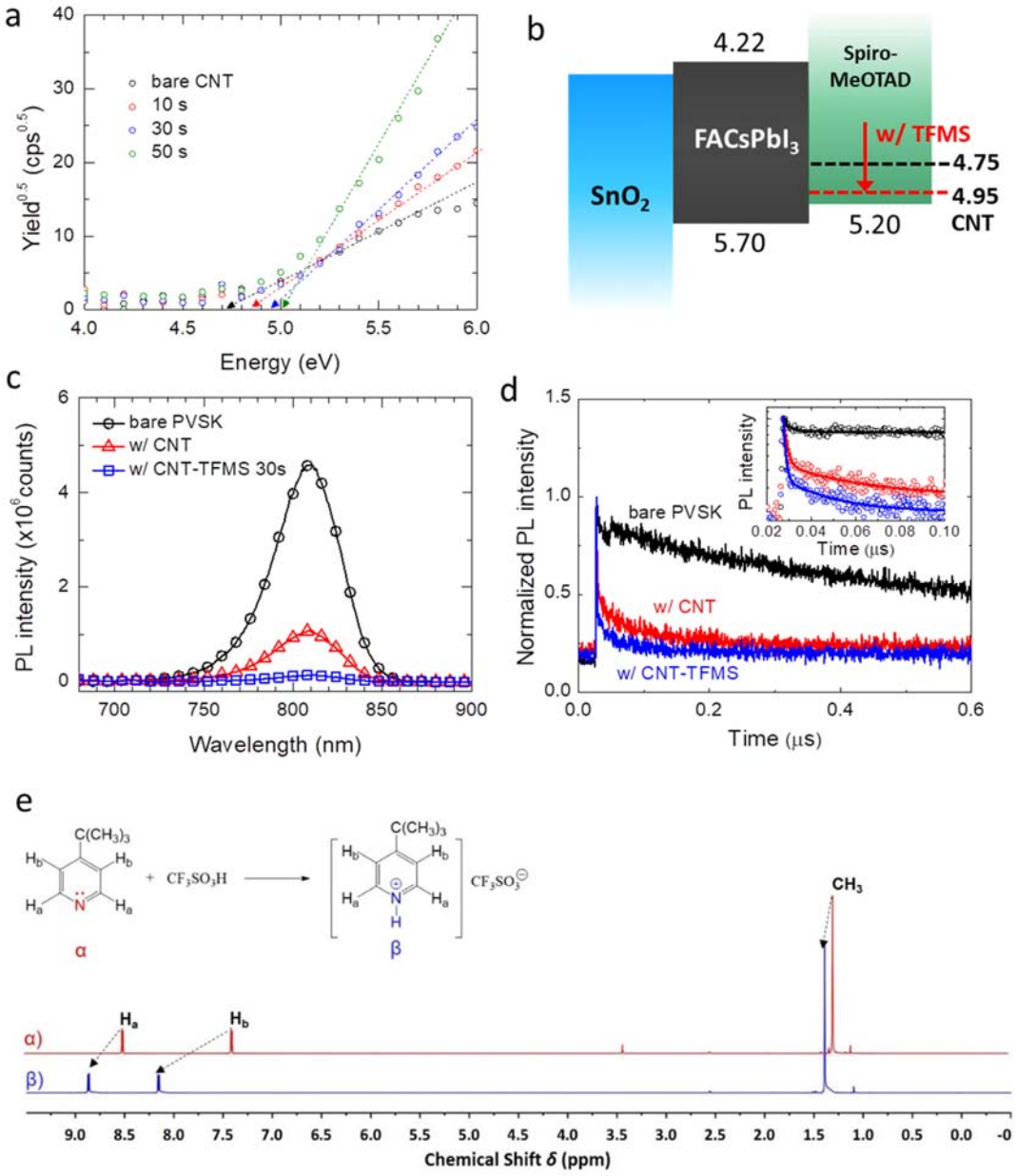

Figure 3. (a) photoelectron yield spectroscopy (PYS) measurement data of bare CNT (black circles), 10 s vapor-doped CNT (red circles), 30 s vapor-doped CNT (blue circles), and 50 s vapor-doped CNT (green circles). The broken lines are the linear fit of the data. (b) Band alignment in the planar heterojunction perovskite solar cells without and with doping of the CNT (c) Steady-state photoluminescence (PL) spectra and (d) time-resolved PL decay profiles of bare perovskite film and perovskite films in contact with bare CNT and CNT doped by TFMS. (e) ^{1}H NMR spectra were recorded in DMSO-d_6 solution at 500 MHz. α) ^{1}H NMR of 4-*tert*-butylpyridine; β) ^{1}H NMR of 4-*tert*-butylpyridine with an addition of 10 wt% of trifluoromethanesulfonic acid.

Thermal- and light-stability test was conducted on bare CNT-PSCs, TFMS-doped CNT-PSCs, and the silver metal electrode-used PSCs as the reference. All three different types of devices were encapsulated under N_2 atmosphere and subjected to the open-circuit under constant illumination of 1 sun (the light was generated by halogen lamps) in air (60±5 °C, relative humidity of 50±10%). The results in **Figure 4a** show that the CNT top electrode-used PSCs are much more stable than the silver electrode-used CNT PSCs of which the degradation can be ascribed to migration of metal ions followed by reaction with perovskite.[9, 18] With a silver electrode, the PCE of the device was degraded by 68.0% from the initial PCE, whereas the CNT based devices retained higher PCE after 244 h of illumination (83.3% of the initial PCE for the bare CNT-PSCs and 86.9% of the initial PCE for the TFMS-doped CNT-PSCs). It was interesting to observe that the TFMS-doped CNT-PSCs were slightly more stable than the bare CNT-PSCs. To investigate the reason behind this phenomenon, water contact angles were measured on CNT films with different vapor doping times (**Figure S8**). The results show that the water contact angle increases upon TFMS vapor doping. This denotes that the application of TFMS makes the CNT electrodes slightly more hydrophobic due possibly to the fluorinated end of TFMS sticking out from CNT.[26] Although the difference is marginal, such an increase in hydrophobicity reduces the intrusion of moisture, which has a direct impact on the stability of the perovskite in a long-term operation. The contact angle decreased when the vapor doping time exceeded 30 s. We conjecture that this is because the charged acidic end of TFMS outweighing the effect of the fluorinated part of TFMS when an excess amount of TFMS is introduced.

Water vapor transmittance rate (WVTR) measurement was used to further investigate the water transmitting property. According to **Figure 4b**, The 30 s TFMS vapor-doped CNT film shows a slightly lower WVTR value than the bare CNT film. For the CNT film with the 50 s TFMS vapor

doping, WVTR value is slightly higher than the bare CNT film, supporting our claim about the hydrophobicity of the CNT films. Although the WVTR value difference is small, the accumulated amount of transmitted water makes a substantial difference over a long period of time (inset of **Figure 4b**). This must have led to the difference in the stability between the TFMS-doped CNT-PSCs and the bare CNT-PSCs. We also suspect the charge extraction may have influenced the stability. As discussed above, the TFMS-doped CNTs have a better energy alignment with a lower V_{OC} loss than the bare CNT-PSCs. Since not all of the uncollected charge gets recombined, delocalized charge within the perovskite system can accelerate the trapped charge-driven degradation.[27]

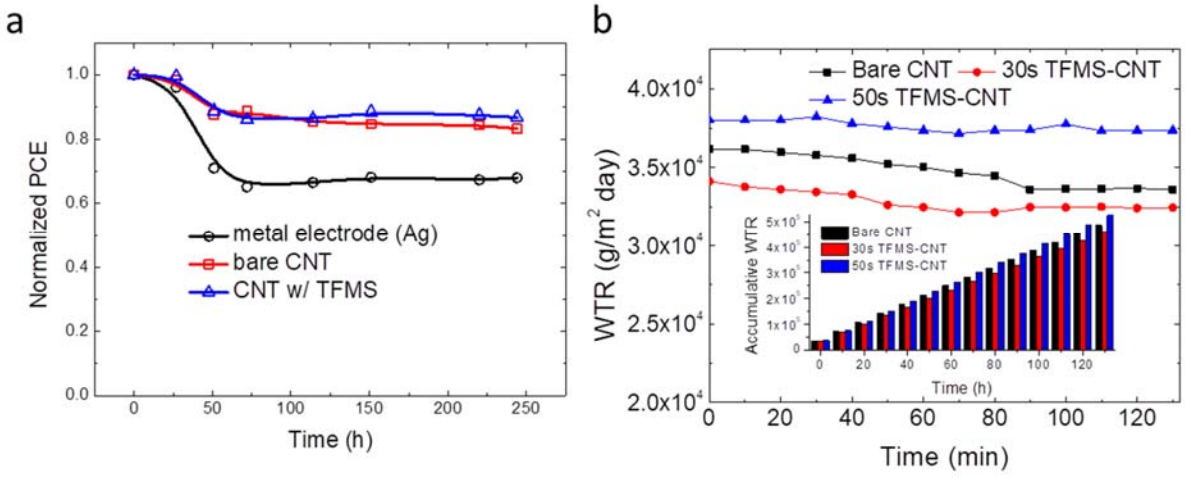

Figure 4. (a) Evolution of power conversion efficiency (PCE) of the encapsulated devices under continuous one sun illumination generated by halogen lamps. The devices were under open-circuit condition (T=60±5 °C, relative humidity of 50±10%). (b) Water vapor transmittance rates (WVTRs) of bare CNT (black) film, 30 s vapor-doped CNT film (red), and 50 s vapor-doped CNT film (blue).

In summary, we introduced an effective ex-situ vapor-assisted doping of a CNT top electrode for implementation of efficient and stable perovskite solar cells. The ex-situ TFMS vapor doing enabled enhancement of conductivity with a favorable alignment of work function without

damaging underneath hole transporting and perovskite layers. Owing to enhanced conductivity with a favorable energy alignment, we achieved a PCE of 17.56% with enhanced stability from CNT electrode-laminated PSCs. It is worth mentioning that our method is simple, quick and readily applicable to large area module process. As the record-high PCE showcases, we successfully provided a solution to overcoming the efficiency limit in CNT-laminated PSCs. We believe this method can pave the pathway to higher performance and more stable CNT-incorporated PSCs.

METHODS

Synthesis of CNT sheets and vapor-assisted doping. CNT films were synthesized by an aerosol (floating catalyst) CVD method based on ferrocene vapor decomposition in a CO atmosphere. The catalyst precursor was vaporized by passing through a cartridge filled with ferrocene powder. The flow containing ferrocene vapor was then introduced into the high-temperature zone of a ceramic tube reactor through a water-cooled probe and mixed with additional CO. To obtain stable growth of CNTs, a controlled amount of CO_2 was mixed with the CO carbon source. CNTs were directly collected downstream of the reactor by filtering the flow through a nitrocellulose or silver membrane filter (Millipore Corp., USA; HAWP, 0.45 μm pore diameter). The CNT films were vapor-doped by placing in the fume of TFMS for a designated time before transferring onto perovskite devices.

Materials Characterizations. Surface morphology and elemental distribution analyses of the CNT film was performed by scanning electron microscopy (SEM, Nova Nano 230). Steady-state photoluminescence (PL) spectrum was acquired by a Horiba Jobin Yvon system. A 640 nm monochromatic laser was used to excite the samples. Time-resolved PL decay profiles were

recorded using a Picoharp 300 with time-correlated single-photon counting capabilities. The films were excited by a 640 nm pulse laser with a repetition frequency of 100 kHz provided by a picosecond laser diode head (PLD 800B, PicoQuant). The power of the excitation light was controlled to be ca. 1.4 nJ/cm^2 to minimize the carrier annihilation and non-geminate recombination. The Fermi levels were measured by Riken Keiki photoelectron yield spectroscopy in air (PYS-A) AC-2 and kelvin probe S spectroscopy in air (ESA). They were calibrated by Au before the measurement. WVTR measurement was carried out by Sumitomo Chemical Co. Ltd. Four probe was measured by a home-built system. Shimadzu UV-3150 was used for the UV-vis measurement. Solartron SI1287 Electrochemical Interface and Solartron 1255B Frequency Response Analyzer were used for the Impedance Measurement.

Device fabrication. Indium doped tin oxide (ITO) glass substrates were cleaned with successive sonication in detergent, deionized (DI) water, acetone and 2-propanol baths for 15 min respectively. The cleaned substrates underwent the UV-ozone for enhanced wettability. 30 mM $SnCl_2 \cdot 2H_2O$ (Aldrich, >99.995%) solution was prepared in ethanol (anhydrous, Decon Laboratories Inc.) as a precursor solution for deposition of a compact SnO_2 layer. The solution was filtered by 0.2 μm syringe filter, followed by spin-coating on the cleaned substrate at 3000 rpm for 30 s. The spin coated film was annealed at 150 ºC for 30 min. After cooling down to room temperature, another cycle of the spin-coating process was repeated, which was followed by annealing at 150 ºC for 5 min and 180 ºC for 1 h. The SnO_2 coated ITO glass was treated with UV-ozone before spin-coating of perovskite solution. The perovskite layer was prepared by the adduct approach.[28-29] Typically,

163.0 mg of $HC(NH_2)_2$ (FAI), 453.4 mg of PbI_2 (TCI, 99.99%), 8.2 mg of PEAI, 5.0 mg of CsI (Alfa Aesar, 99.999%) and 97.4 mg of N-Methyl-2-pyrrolidone (NMP, Sigma-Aldrich, anhydrous, 99.5%) were added to 560 mg of N,N-Dimethylformamide (DMF, Sigma-Aldrich, anhydrous, 99.8%). Perovskite and hole transporting layer was formed in a glove box filled with dry air. The perovskite solution was spin-coated at 4000 rpm for 20 s to which 0.15 mL of diethyl ether (anhydrous, >99.0%, contains BHT as stabilizer, Sigma-Aldrich) was dropped after 10 s. The resulting transparent adduct film was heat-treated at 80 ºC for 1 min followed by 150 ºC for 20 min. The spiro-MeOTAD solution was prepared by dissolving 85.8 mg of spiro-MeOTAD (Lumtec) in 1 mL of chlorobenzene (anhydrous, 99.8%, Sigma-Aldrich) which was mixed with 33.8 μl of 4-tert-butylpyridine (96%, Aldrich) and 19.3 μl of Li-TFSI (99.95%, Aldrich, 520 mg/mL in acetonitrile) solution. The CNT film was laminated onto the perovskite film, and a supporting nitrocellulose film was removed after the limination. The spiro-MeOTAD solution was applied onto the CNT layer to improve the contact between the CNTs and the perovskite. The spiro-MeOTAD solution was spin-coated on the perovskite layer at 3000 rpm for 20 s by dropping 17 μl of the solution during the spinning. For deposition of a metal electrode, an approximately 100 nm-thick silver layer was thermally evaporated at 0.5 Å/s on top of the spiro-MeOTAD layer.

Device characterizations. Current density-voltage (*J–V*) curves of the devices were recorded using Keithley 2401 source meter under simulated one sun illumination (AM 1.5G, 100 mW/cm^2) generated from Oriel Sol3A with class AAA solar simulator (Newport). The intensity of the light was calibrated by NREL-certified Si photodiode equipped with KG-5 filter. The *J–V* curves were recorded at 0.1 V/s (between 1.2 V and -0.1 V with 65 data points and 0.2 s of delay time per point). The devices were covered with metal aperture with an area of 0.100 cm^2 to define the active

area during the measurement. All the devices were measured without pre-conditioning (light-soaking and/or applied bias voltage.

ASSOCIATED CONTENT

The Supporting Information is available free of charge on the ACS Publications website.

AUTHOR INFORMATION

Corresponding Author

*Corresponding authors

Y. M. E-mail: matsuo@photon.t.u-tokyo.ac.jp

S. M. E-mail: maruyama@photon.t.u-tokyo.ac.jp

Y. Y. E-mail: yangy@ucla.edu

Author Contributions

‡These authors contributed equally.

Notes

The authors declare no competing financial interest.

ACKNOWLEDGMENT

This work was supported by Air Force Office of Scientific Research (AFOSR, Grant No. FA9550-15-1-0333), Office of Naval Research (ONR, Grant No. N00014-17-1-2484), National Science Foundation (NSF, Grant No. ECCS-EPMD-1509955), and Horizon PV. I.J gratefully acknowledge the Research and Education Consortium for Innovation of Advanced Integrated

Science by Japan Science and Technology (JST) and Japan Society for the Promotion of Science (JSPS) KAKENHI Grant Numbers JP15H05760, JP16H02285, 17K04970, and 17H06609.

REFERENCES

1. Kojima, A.; Teshima, K.; Shirai, Y.; Miyasaka, T., Organometal halide perovskites as visible-light sensitizers for photovoltaic cells. *J. Am. Chem. Soc.* **2009,** *131* (17), 6050-6051.
2. Im, J.-H.; Lee, C.-R.; Lee, J.-W.; Park, S.-W.; Park, N.-G., 6.5% efficient perovskite quantum-dot-sensitized solar cell. *Nanoscale* **2011,** *3* (10), 4088-4093.
3. Kim, H.-S.; Lee, C.-R.; Im, J.-H.; Lee, K.-B.; Moehl, T.; Marchioro, A.; Moon, S.-J.; Humphry-Baker, R.; Yum, J.-H.; Moser, J. E., Lead iodide perovskite sensitized all-solid-state submicron thin film mesoscopic solar cell with efficiency exceeding 9%. *Sci. Rep.* **2012,** *2*, 591.
4. Lee, M. M.; Teuscher, J.; Miyasaka, T.; Murakami, T. N.; Snaith, H. J., Efficient hybrid solar cells based on meso-superstructured organometal halide perovskites. *Science* **2012,** *338* (6107), 643-647.
5. National renewable energy laboratory, Best research-cell efficiency chart, https://www.nrel.gov/pv/assets/images/efficiency-chart.png.
6. Song, Z.; McElvany, C. L.; Phillips, A. B.; Celik, I.; Krantz, P. W.; Watthage, S. C.; Liyanage, G. K.; Apul, D.; Heben, M. J., A technoeconomic analysis of perovskite solar module manufacturing with low-cost materials and techniques. *Energy Environ. Sci.* **2017,** *10* (6), 1297-1305.
7. Gong, J.; Darling, S. B.; You, F., Perovskite photovoltaics: life-cycle assessment of energy and environmental impacts. *Energy Environ. Sci.* **2015,** *8* (7), 1953-1968.
8. Kato, Y.; Ono, L. K.; Lee, M. V.; Wang, S.; Raga, S. R.; Qi, Y., Silver iodide formation in methyl ammonium lead iodide perovskite solar cells with silver top electrodes. *Advanced Materials Interfaces* **2015,** *2* (13).
9. Domanski, K.; Correa-Baena, J.-P.; Mine, N.; Nazeeruddin, M. K.; Abate, A.; Saliba, M.; Tress, W.; Hagfeldt, A.; Grätzel, M., Not all that glitters is gold: Metal-migration-induced degradation in perovskite solar cells. *ACS nano* **2016,** *10* (6), 6306-6314.
10. Habisreutinger, S. N.; Nicholas, R. J.; Snaith, H. J., Carbon Nanotubes in Perovskite Solar Cells. *Adv. Energy Mater.* **2017,** *7* (10).
11. Habisreutinger, S. N.; Leijtens, T.; Eperon, G. E.; Stranks, S. D.; Nicholas, R. J.; Snaith, H. J., Carbon nanotube/polymer composites as a highly stable hole collection layer in perovskite solar cells. *Nano Lett.* **2014,** *14* (10), 5561-5568.
12. Jeon, I.; Matsuo, Y.; Maruyama, S., Single-Walled Carbon Nanotubes in Solar Cells. *Top. Curr. Chem.* **2018,** *376* (1), 4.
13. Habisreutinger, S. N.; Wenger, B.; Snaith, H. J.; Nicholas, R. J., Dopant-free planar n–i–p perovskite solar cells with steady-state efficiencies exceeding 18%. *ACS Energy Lett.* **2017,** *2* (3), 622-628.

14. Kaskela, A.; Nasibulin, A. G.; Timmermans, M. Y.; Aitchison, B.; Papadimitratos, A.; Tian, Y.; Zhu, Z.; Jiang, H.; Brown, D. P.; Zakhidov, A., Aerosol-synthesized SWCNT networks with tunable conductivity and transparency by a dry transfer technique. *Nano Lett.* **2010,** *10* (11), 4349-4355.
15. Nasibulin, A. G.; Kaskela, A.; Mustonen, K.; Anisimov, A. S.; Ruiz, V.; Kivisto, S.; Rackauskas, S.; Timmermans, M. Y.; Pudas, M.; Aitchison, B., Multifunctional free-standing single-walled carbon nanotube films. *ACS nano* **2011,** *5* (4), 3214-3221.
16. Li, Z.; Kulkarni, S. A.; Boix, P. P.; Shi, E.; Cao, A.; Fu, K.; Batabyal, S. K.; Zhang, J.; Xiong, Q.; Wong, L. H., Laminated carbon nanotube networks for metal electrode-free efficient perovskite solar cells. *ACS nano* **2014,** *8* (7), 6797-6804.
17. Aitola, K.; Sveinbjörnsson, K.; Correa-Baena, J.-P.; Kaskela, A.; Abate, A.; Tian, Y.; Johansson, E. M.; Grätzel, M.; Kauppinen, E. I.; Hagfeldt, A., Carbon nanotube-based hybrid hole-transporting material and selective contact for high efficiency perovskite solar cells. *Energy Environ. Sci.* **2016,** *9* (2), 461-466.
18. Aitola, K.; Domanski, K.; Correa-Baena, J. P.; Sveinbjörnsson, K.; Saliba, M.; Abate, A.; Grätzel, M.; Kauppinen, E.; Johansson, E. M.; Tress, W., High Temperature-Stable Perovskite Solar Cell Based on Low-Cost Carbon Nanotube Hole Contact. *Adv. Mater.* **2017,** *29* (17).
19. Ahn, N.; Jeon, I.; Yoon, J.; Kauppinen, E. I.; Matsuo, Y.; Maruyama, S.; Choi, M., Carbon-sandwiched perovskite solar cell. *J. Mater. Chem. A* **2018**.
20. Jeon, I.; Delacou, C.; Kaskela, A.; Kauppinen, E. I.; Maruyama, S.; Matsuo, Y., Metal-electrode-free window-like organic solar cells with p-doped carbon nanotube thin-film electrodes. *Sci. Rep.* **2016,** *6*, 31348.
21. Han, T. H.; Kwon, S. J.; Li, N.; Seo, H. K.; Xu, W.; Kim, K. S.; Lee, T. W., Versatile p-Type Chemical Doping to Achieve Ideal Flexible Graphene Electrodes. *Angew. Chem. Int. Ed.* **2016,** *55* (21), 6197-6201.
22. Cui, K.; Qian, Y.; Jeon, I.; Anisimov, A.; Matsuo, Y.; Kauppinen, E. I.; Maruyama, S., Scalable and Solid-State Redox Functionalization of Transparent Single-Walled Carbon Nanotube Films for Highly Efficient and Stable Solar Cells. *Adv. Energy Mater.* **2017,** *7* (18).
23. Jeon, I.; Cui, K.; Chiba, T.; Anisimov, A.; Nasibulin, A. G.; Kauppinen, E. I.; Maruyama, S.; Matsuo, Y., Direct and dry deposited single-walled carbon nanotube films doped with MoO x as electron-blocking transparent electrodes for flexible organic solar cells. *J. Am. Chem. Soc.* **2015,** *137* (25), 7982-7985.
24. Marziano, N. C.; Ronchin, L.; Tortato, C.; Zingales, A.; Sheikh-Osman, A. A., Acidity and reactivity of trifluoromethanesulfonic acid in liquid and solid acid catalysts. *J. Mol. Catal. A: Chem.* **2001,** *174* (1-2), 265-277.
25. Jeon, I.; Ueno, H.; Seo, S.; Aitola, K.; Nishikubo, R.; Saeki, A.; Okada, H.; Boschloo, G.; Maruyama, S.; Matsuo, Y., Lithium-Ion Endohedral Fullerene (Li+@ C60) Dopants in Stable Perovskite Solar Cells Induce Instant Doping and Anti-Oxidation. *Angew. Chem.* **2018**.

26. Du Toit, F.; Sanderson, R.; Engelbrecht, W.; Wagener, J., The effect of surface fluorination on the wettability of high density polyethylene. *J. Fluorine Chem.* **1995,** *74* (1), 43-48.
27. Ahn, N.; Kwak, K.; Jang, M. S.; Yoon, H.; Lee, B. Y.; Lee, J.-K.; Pikhitsa, P. V.; Byun, J.; Choi, M., Trapped charge-driven degradation of perovskite solar cells. *Nat. Commun.* **2016,** *7*, 13422.
28. Lee, J.-W.; Kim, H.-S.; Park, N.-G., Lewis Acid–Base Adduct Approach for High Efficiency Perovskite Solar Cells. *Acc. Chem. Res.* **2016,** *49* (2), 311-319.
29. Lee, J.-W.; Dai, Z.; Lee, C.; Lee, H. M.; Han, T.-H.; De Marco, N.; Lin, O.; Choi, C. S.; Dunn, B.; Koh, J.; Di Carlo, D.; Ko, J. H.; Maynard, H. D.; Yang, Y., Tuning Molecular Interactions for Highly Reproducible and Efficient Formamidinium Perovskite Solar Cells via Adduct Approach. *J. Am. Chem. Soc.* **2018**.

Supporting Information

Overcoming Efficiency Limits of Carbon Nanotube –Laminated Metal-free Perovskite Solar Cells

Jin-Wook Lee[‡1], Il Jeon[‡2], Haosheng Lin[2], Seungju Seo,[2] Tae-Hee Han[1], Anton Anisimov[3], Esko I. Kauppinen[4], Yutaka Matsuo[2], Shigeo Maruyama*[2,5], Yang Yang*[1]*

[1]Department of Materials Science and Engineering and California Nano Systems Institute, University of California, Los Angeles, CA 90095, United States

[2]Department of Mechanical Engineering, School of Engineering, The University of Tokyo, Tokyo 113-8656, Japan

[3]Canatu, Ltd., Konalankuja 5, FI-00390 Helsinki, Finland

[4]Department of Applied Physics, Aalto University School of Science, FI-00076 Aalto, Finland

[5]Energy Nano Engineering Laboratory, National Institute of Advanced Industrial Science and Technology (AIST), Ibaraki 305-8564, Japan

[‡]These authors contributed equally to this work.

Y. M. E-mail: matsuo@photon.t.u-tokyo.ac.jp

S. M. E-mail: maruyama@photon.t.u-tokyo.ac.jp

Y. Y. E-mail: yangy@ucla.edu; TEL: +1-310-825-4052

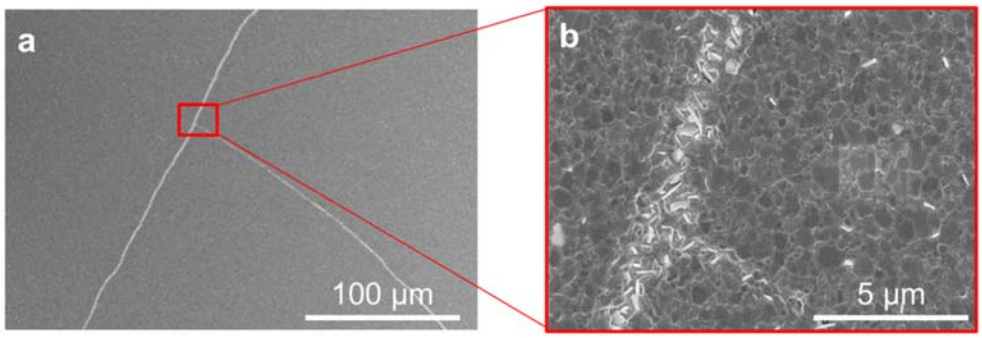

Figure S1. SEM images of 2D/3D FACsPbI$_3$ film forming cracks after excessive force was applied during the CNT lamination step.

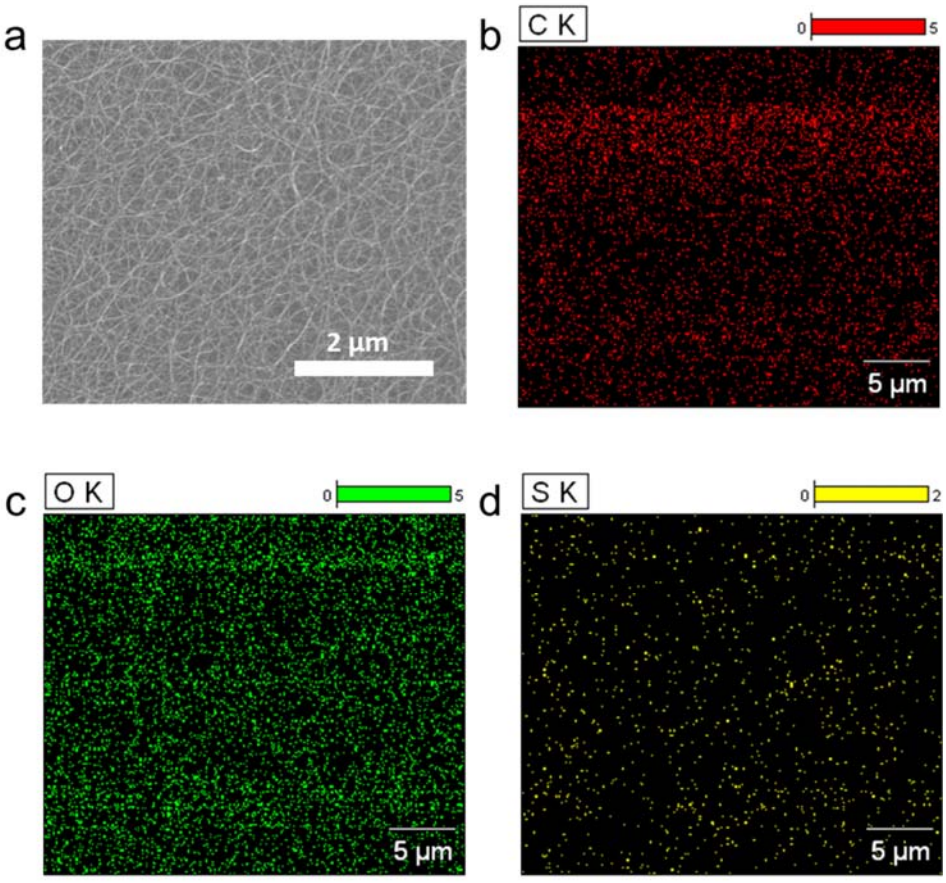

Figure S2. (a) Scanning microscopic image of the TFMS doped CNT. Elemental distribution analysis of the CNT; (b) carbon, (c) oxygen and (d) sulfur.

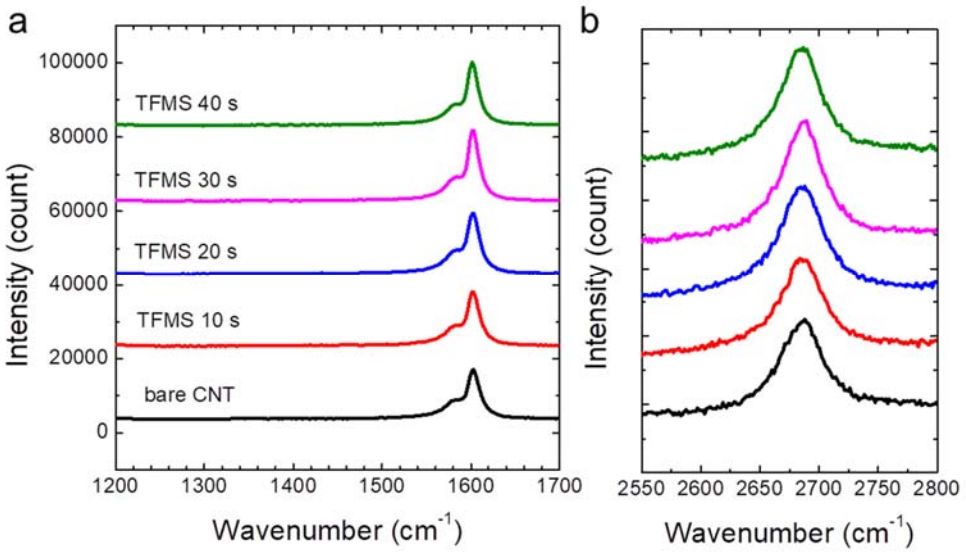

Figure S3. Raman scattering spectra of the CNT sheets with different exposure time to TFMS vapor. (a) low wavenumber (G-band) and (b) high wavenumber (G′-band) region.

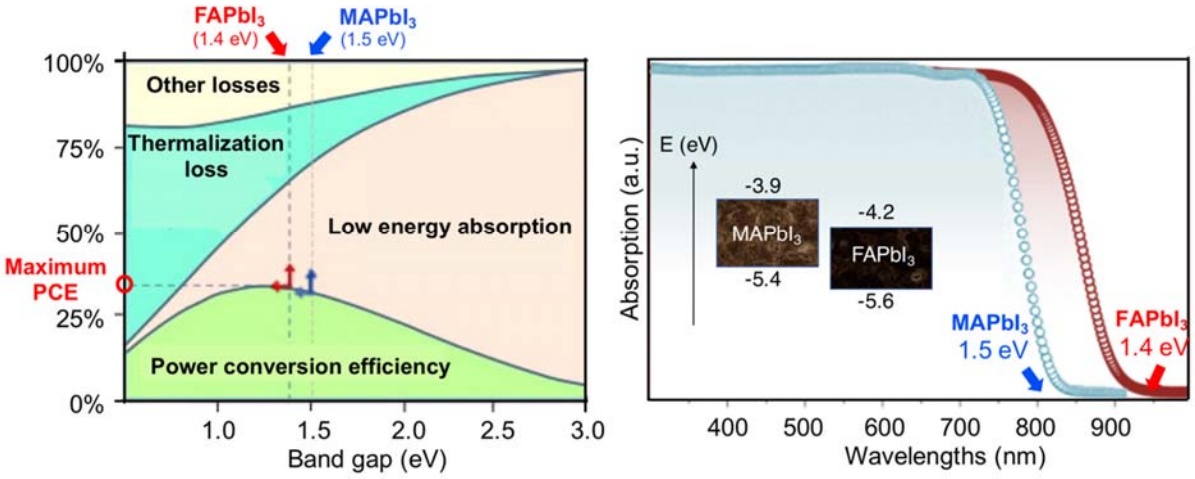

Figure S4. Graph depicting the relationship between Shockley-Queisser limit and the perovskite materials (left), and illustration of UV-vis absorption spectra of $MAPbI_{33}$ and $FAPbI_3$ with their energy levels as an inset (right).

Table S1. Photovoltaic performance of PSCs with metal and CNT electrodes using different perovskite materials under 1 sun (AM 1.5 G, 100 mW cm^{-2}).

Electrode	Perovskite	J_{SC} (mA/cm^2)	V_{OC} (V)	FF	PCE (%)
Au	$MAPbI_3$	23.0	1.08	0.72	17.9
	2D/3D $FACsPbI_3$	25.3	1.06	0.72	20.2
Bare CNT	$MAPbI_3$	21.0	1.05	0.66	14.6
	2D/3D $FACsPbI_3$	23.4	0.99	0.69	15.8

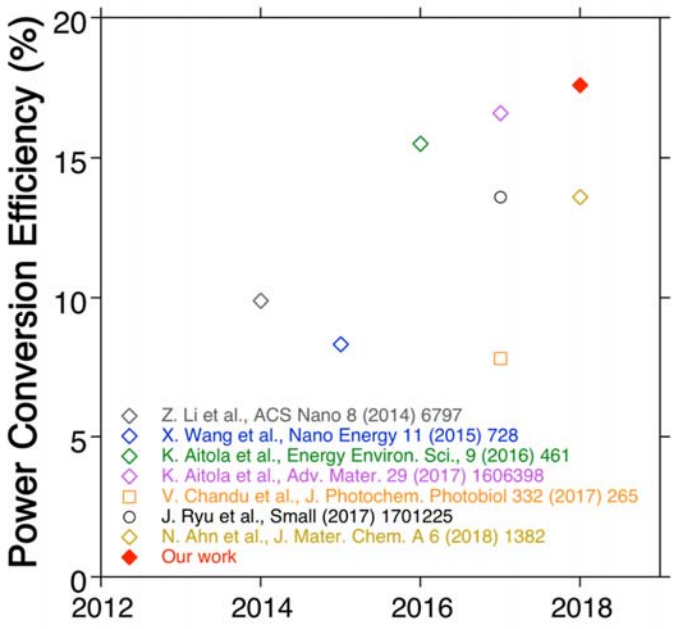

Figure S5. Comparison of the PCEs reported from CNT top electrode-laminated perovskite solar cells.

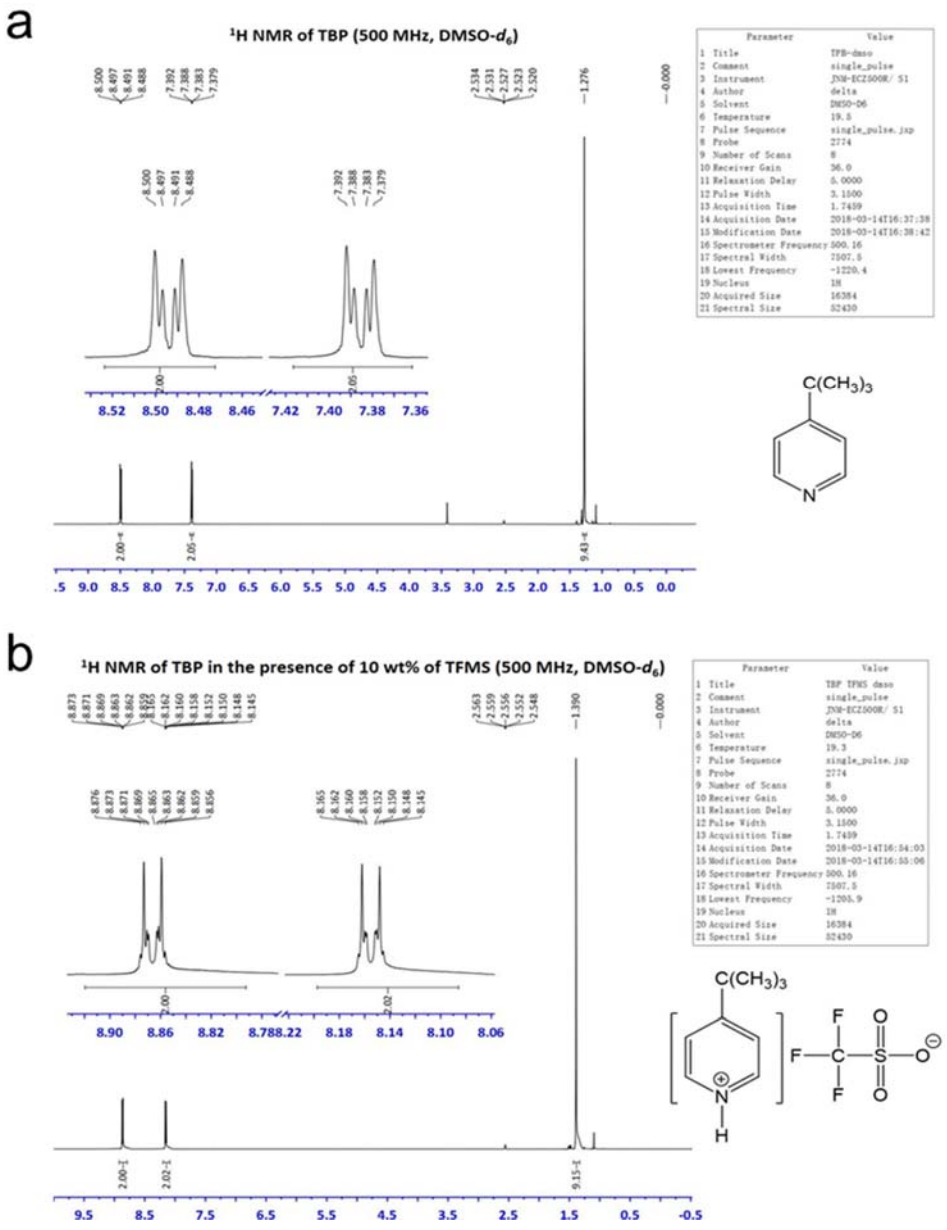

Figure S6. [1]H NMR spectra of (a) *t*-BP and (b) TFMS in DMSO-d$_6$ solution at 500 MHz.

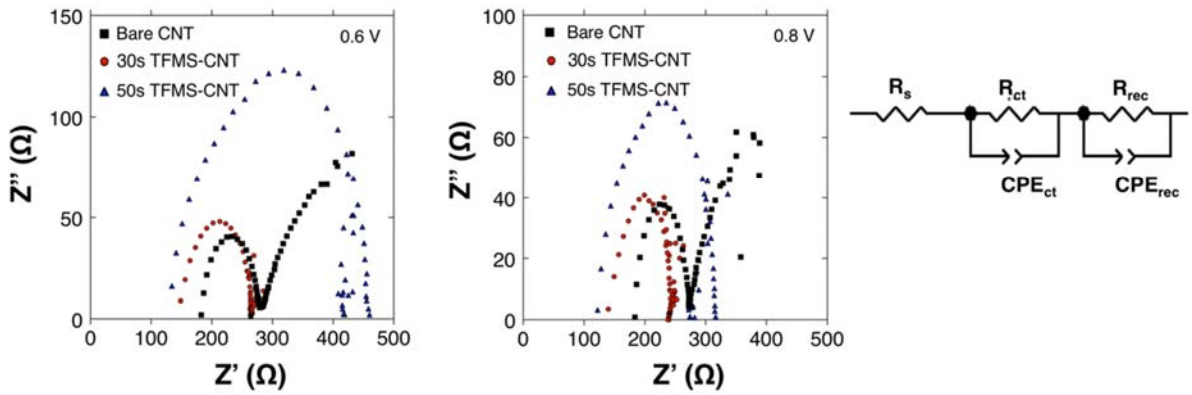

Figure S7. Nyquist plots from the impedance measurement of bare CNT (black sqaure), 30 s TFMS-CNT (red circle), and 50 s TFMS-CNT (blue triangle) at (a) voltage equals to 0.6V and (b) 0.8V with the circuit model on the right.

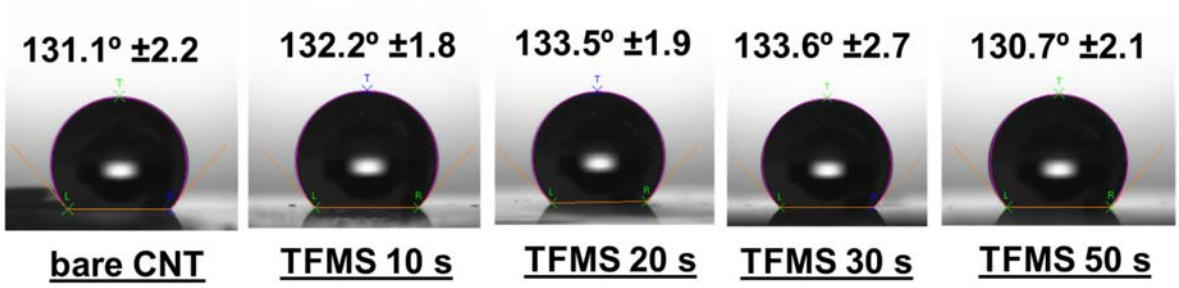

Figure S8. Water contact angles of CNT films with various doping time, showing wettability of CNT surface.